IOP PUBLISHING JOURNAL OF PHYSICS D: APPLIED PHYSICS

J. Phys. D: Appl. Phys. **41** (2008) 155009 (8pp) doi:10.1088/0022-3727/41/15/155009

Microstructure and random magnetic anisotropy in Fe–Ni based nanocrystalline thin films

Senoy Thomas[1], S H Al-Harthi[2], D Sakthikumar[3], I A Al-Omari[2], R V Ramanujan[4], Yasuhiko Yoshida[3] and M R Anantharaman[1,5]

[1] Department of Physics, Cochin University of Science and Technology, Cochin, India-682022
[2] Department of Physics, College of Science, Sultan Qaboos University, PO Box 36, Postal Code 123, Muscat, Sultanate of Oman
[3] Bio-Nano Electronics Research Centre, Department of Applied Chemistry, Toyo University, Kawagoe, Saitama 350-8585, Japan
[4] School of Materials Science and Engineering, Nanyang Avenue, Nanyang Technological University, Singapore 639798, Singapore

E-mail: senoythomas@yahoo.co.in and mra@cusat.ac.in

Received 25 April 2008, in final form 4 June 2008
Published 17 July 2008
Online at stacks.iop.org/JPhysD/41/155009

Abstract

Nanocrystalline Fe–Ni thin films were prepared by partial crystallization of vapour deposited amorphous precursors. The microstructure was controlled by annealing the films at different temperatures. X-ray diffraction, transmission electron microscopy and energy dispersive x-ray spectroscopy investigations showed that the nanocrystalline phase was that of Fe–Ni. Grain growth was observed with an increase in the annealing temperature. X-ray photoelectron spectroscopy observations showed the presence of a native oxide layer on the surface of the films. Scanning tunnelling microscopy investigations support the biphasic nature of the nanocrystalline microstructure that consists of a crystalline phase along with an amorphous phase. Magnetic studies using a vibrating sample magnetometer show that coercivity has a strong dependence on grain size. This is attributed to the random magnetic anisotropy characteristic of the system. The observed coercivity dependence on the grain size is explained using a modified random anisotropy model.

(Some figures in this article are in colour only in the electronic version)

1. Introduction

Nanocrystalline magnetic materials are increasingly becoming a hot topic of research because of their potential in finding end uses in fields such as power electronics, sensors, actuators, soft underlayers for perpendicular recording media and as a core material for writing elements in the modern recording heads [1–3]. The microstructure of these materials consists of nano-sized ferromagnetic materials embedded in an amorphous matrix. The matrix phase must also be ferromagnetic for facilitating the exchange coupling between the nanoparticles. As a result of this coupling, they often exhibit vanishing magnetocrystalline anisotropy. Since the soft magnetic properties are strongly related to the crystalline anisotropy, the exchange interaction in nanocrystalline magnetic materials results in an improvement in soft magnetic properties.

The averaging out of magnetocrystalline anisotropy in these materials can be explained in terms of the random anisotropy model proposed by Alben *et al* [4]. The effective anisotropy energy density in this model is given by the square root of the mean square fluctuation of the anisotropy energy in the exchange coupled volume. Although the random anisotropy model was propounded to explain the magnetic softness in amorphous materials, Herzer showed that the model is also applicable to nanocrystalline systems [5].

For an assembly of ferromagnetically coupled grains of size D ($D < L_{ex}$) with randomly oriented magnetocrystalline

[5] Author to whom any correspondence should be addressed.

anisotropies K_1, the average anisotropy $\langle K \rangle$ is given by $\langle K \rangle = K_1(D/(A/K_1)^{1/2})^{2n/(4-n)}$ [6] where n denotes the dimension of the system. This means that $\langle K \rangle$ follows a $D^{2/3}$, D^2 and D^6 dependence on the grain size for one-dimensional, two-dimensional and three-dimensional structures, respectively. The coercivity (H_c) and permeability (μ) are related to $\langle K \rangle$ through the relation $H_c \propto \langle K \rangle$ and $\mu \propto 1/\langle K \rangle$.

The sensitive grain size dependence on the soft magnetic properties in these materials is related to the interplay of local magnetocrystalline anisotropy energy and the ferromagnetic exchange interaction. For large grains the magnetization can follow the local easy magnetic directions and the magnetization process is determined by the magnetocrystalline anisotropy K_1 of the crystallites. However, for very small grains, the ferromagnetic exchange interaction forces the magnetic moments to align parallel to each other. Thus, the effective anisotropy will be an average over several grains and will be reduced in magnitude. The dividing line between these two extremes is the ferromagnetic exchange correlation length $L_{ex} = (A/K_1)^{1/2}$, where A is the exchange stiffness constant and K_1 is the anisotropy constant.

Amorphous alloys which are precursors to nanocrystalline materials can be synthesized by a variety of techniques such as rapid solidification from the liquid state, mechanical alloying, plasma processing and vapour deposition [7]. Nanocrystalline microstructures can be obtained by the controlled crystallization of the amorphous state. There are several reports in the literature pertaining to this method of preparation [8–11]. Melt quenching or high energy ball milling was used for preparing metastable states and most of the studies were carried out in ribbons or in powders. With the advent of nanocrystalline materials exhibiting excellent soft magnetic properties thin films of these materials are also important from an application point of view.

Vapour deposition offers a simple alternative for sputter deposition in obtaining thin films of supersaturated solid solutions and other metastable states. Amorphous magnetic thin films thus obtained presents high coercivity due to the stresses in the films. This makes them unsuitable for soft magnetic applications. One way of improving the magnetic softness is by precipitating nanocrystals within the amorphous matrix. Further nanocrystallization allows one to tailor the magnetic properties by controlling the size of the precipitates. Control of magnetic properties is highly essential in order to obtain miniaturized magnetic devices with improved performance characteristics. Since the magnetic properties are strongly dependent on the microstructure, the soft magnetic properties can be tuned by modifying the microstructure.

METGLAS 2826 MB ($Fe_{40}Ni_{38}Mo_4B_{18}$) is a soft magnetic alloy that exhibits superior soft magnetic properties. Its softness after nanocrystallization can be ascribed to its two phase nature consisting of Fe–Ni nanocrystals embedded in the remaining boron rich amorphous matrix. Additives such as boron and molybdenum are incorporated in the alloy to achieve specific objectives. Boron aids in retaining the glassy characteristics while molybdenum is a known grain growth inhibitor. However, high metalloid content causes deterioration not only in magnetic properties but also in elasticity and plasticity [12]. If B and Mo can be dispensed within FeNi-based alloys such as METGLAS, this is economical and is an attractive proposition from a commercial point of view. Since METGLAS is widely used for sensor applications, the thin film form of this material would be of considerable interest for integrating thin film sensors with today's microelectronics. This can be realized by depositing thin films of this material on suitable substrates.

Some attempts of preparation of METGLAS thin films by thermal evaporation have been reported in the literature [13, 14]. Thin films of $Fe_{40}Ni_{38}Mo_4B_{18}$ were prepared by the flash evaporation technique [13]. The electron microscopy and diffraction investigations on these films showed that the films decompose in a eutectic fashion with thermal annealing. Magnetic studies were not carried out on the samples and the main focus of the paper was on structural evolution of these films with thermal annealing. An alloy film with the same composition was studied by our group [14]. Thin films (thickness around 36 nm) of $Fe_{40}Ni_{38}Mo_4B_{18}$ were prepared by thermally evaporating METGLAS 2826 MB ribbons. The deposited films were amorphous and were thermally annealed to obtain a nanocrystalline microstructure. A lowering in the crystallization temperature was observed (~473 K) when compared with the bulk alloy system (683 K) which was attributed to the lower volume fraction of molybdenum in the thin films. The observed changes in coercivity with annealing temperature were explained using the random anisotropy model extended to two-dimensional systems. However, in these investigations the composition of the film was not ascertained and the nature of the microstructure was not established by any experimental techniques. Such a study only will give credence in correlating the microstructure with magnetic properties. Also, the amorphous interlayer in nanocrystalline magnetic material plays a crucial role in determining the magnetic and electronic properties. Hence, employment of sophisticated techniques such as scanning tunnelling microscopy (STM) and scanning tunnelling spectroscopy (STS) in characterizing the material has significance from an application point of view. Further STS is a powerful tool for investigating inhomogeneity in surface electronic states. It is in this context that a systematic investigation on a magnetic soft alloy based on Fe–Ni assumes significance.

Our main objective in this work is to gain insight into the microstructural evolution with thermal annealing in Fe–Ni based amorphous thin films and to correlate the observed magnetic properties with microstructural evolution. For this we have prepared Fe–Ni based amorphous thin films by the thermal evaporation technique. Nanocrystalline microstructure was obtained by the partial crystallization of the amorphous films. The microstructure was controlled by annealing the films at different temperatures. The films were characterized using the x-ray diffraction (XRD) technique, transmission electron microscopy (TEM), selected area electron diffraction (SAED), energy dispersive x-ray spectroscopy (EDS), x-ray photoelectron spectroscopy (XPS), STM, STS and a vibrating sample magnetometer. Finally

the size evolution of coercivity is explained using a random anisotropy model extended to two-dimensional systems.

2. Experiment

2.1. Preparation

A commercially available METGLAS 2826 MB ribbon of composition $Fe_{40}Ni_{38}Mo_4B_{18}$ was employed as a source material to deposit Fe–Ni thin films on silicon and NaCl substrates. The silicon substrates were cleaned with acetone, ethanol and trichloroethylene and were immediately loaded into the vacuum chamber. The distance from the source to the centre of a 1 cm^2 substrate was 20 cm. The films were deposited by thermal evaporation using a current of 23 A at a pressure of about 1×10^{-5} mbar. The base pressure of $\sim 1 \times 10^{-5}$ mbar was achieved by a diffusion pump backed with a rotary pump. These thin films have also been heat treated at 373, 473, 573 and 673 K to follow microstructural evolution of the as-deposited films. The annealing treatment consisted of increasing the temperature of the samples at about 10 K min^{-1} to the desired temperature, holding it for 1 h and cooling to room temperature. The annealing was performed in a vacuum of 1×10^{-5} mbar.

2.2. Characterization

The thicknesses of the films were determined using scanning electron microscopy cross-sectional measurements (JEOL JSM 6390). XRD measurements were performed using an x-ray powder diffractometer technique employing a copper target (Cu Kα = 1.5418 Å, Rigaku *D*max C). The scanning speed was adjusted to 2° min^{-1} with a sampling interval of 0.05. TEM experiments were carried out on films coated on NaCl substrates. A JEOL JEM-2200 FS electron microscope operating at 200 kV was used for this. The compositions of the films were analysed using an energy dispersive x-ray spectrometer which was attached to the TEM column. XPS measurements were carried out using an Omicron Nanotechnology Multiprobe Instrument. XPS spectra were obtained using a high resolution hemisphere analyzer EA 125 HR equipped with a detection system consisting of seven channeltrons. A monochromated Al Kα source of energy $h\nu$ = 1486.6 eV was used to probe the films which was attached to a molybdenum sample holder. The pressure in the XPS chamber during the measurements was 5×10^{-10} mbar. STM/STS studies were carried out using a Veeco-Digital Instruments multimode scanning probe microscope operated under ambient conditions. All the STM/STS studies reported here were performed using tungsten tips. The STM images were recorded in the constant current mode at a sample bias of 1.2 V and a current set point of 0.4 nA. The topographical images represent the height of the tunnelling tip above the sample. The images presented here are digitally filtered to remove the low frequency noises. Once stable and repetitive images were obtained the instrument was switched into the STS mode to acquire the *I*–*V* characteristics. The STS measurements were carried out by placing the tunnelling tip above a region of interest and keeping the tip–sample separation fixed while recording the *I*–*V* characteristics. The voltage was swept from +1 V to −1 V and the corresponding tunnelling currents were measured. STS was done on different regions on the sample surface to study the inhomogeneity in surface electronic properties. Room temperature magnetization measurements were carried out using a vibrating sample magnetometer (DMS 1660 VSM) with an external field varying from −1 to +1 kOe.

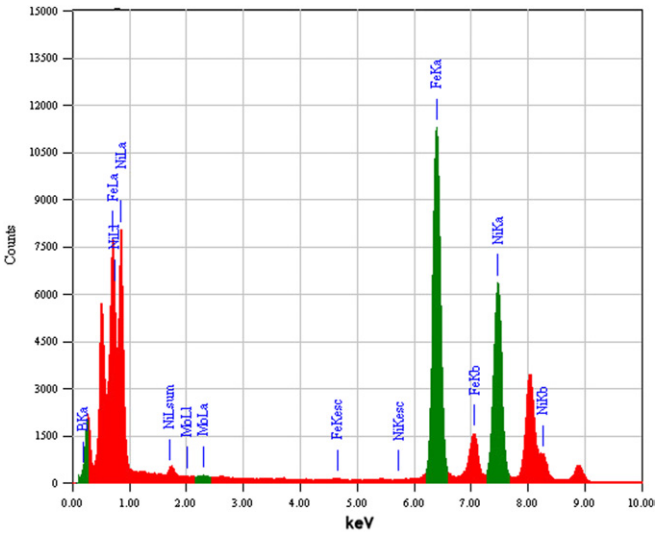

Figure 1. EDS profile for the as-deposited film.

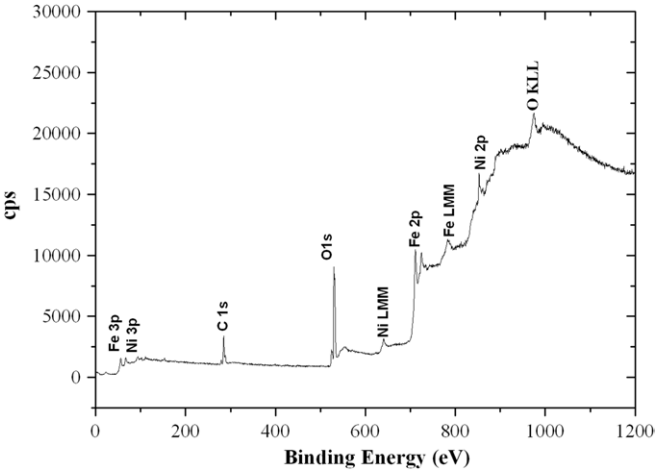

Figure 2. XPS survey scan for the as-deposited film.

2.3. Compositional analysis

Figure 1 shows the energy dispersive x-ray spectrum of the as-deposited film. The composition of the films was measured from the peak intensities of Fe Kα and Ni Kα lines in the EDS spectrum after background subtraction. The atomic percentage of Fe and Ni were 55 and 45, respectively. An XPS survey scan was collected for the as-deposited film and is depicted in figure 2. The spectrum exhibits characteristic photoelectron lines of Fe, Ni, O and C. The C 1s peak corresponds to the unavoidable contaminant carbon on the top surface of the specimen. The O 1s spectrum consists of the peak originating from oxygen in the metal–oxygen bond. The survey scan

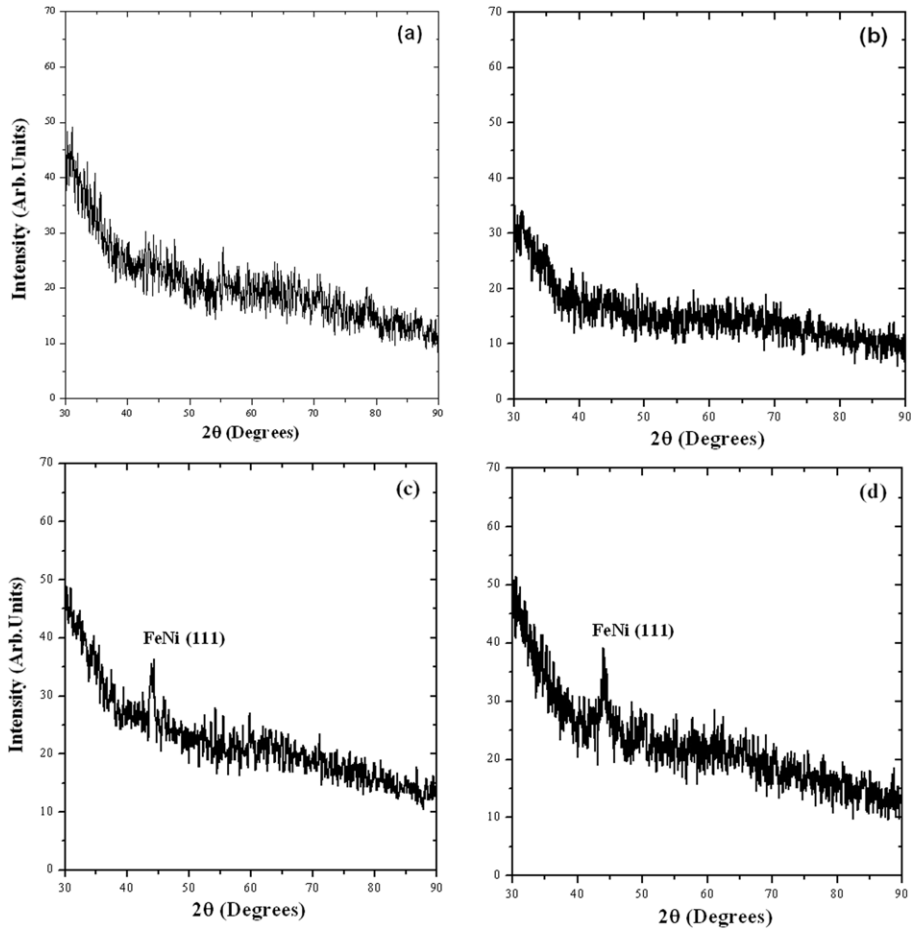

Figure 3. XRD pattern of (*a*) as-deposited film and films annealed at (*b*) 373 K, (*c*) 473 K and (*d*) 573 K.

also exhibited lines corresponding to the emission of Auger electrons (Ni LMM, Fe LMM and O KLL). In XPS the relative sensitivities of Fe, Mo and B when compared with Ni are 0.86, 0.64 and 0.06, respectively. Boron and molybdenum were not detected in the EDS as well as in the XPS survey scan. The absence of molybdenum and boron in both EDS and XPS indicates that the film is deficient in boron and molybdenum. This is expected because out of the four elements Fe, Ni, Mo and B, boron and molybdenum have the highest melting point and lowest vapour pressures. So it is believed that boron and molybdenum are not getting evaporated from the target material.

2.4. Structural and microstructural characterization

Cross-sectional SEM images showed that the films were of 25 nm thickness. The XRD pattern of as-deposited and annealed films is depicted in figure 3. The XRD pattern of the as-deposited thin film does not show any sharp diffraction peaks indicating that they are amorphous. The amorphous state is stable up to a temperature of 373 K. The onset of nanocrystallization is at around 473 K. It should be noted that in METGLAS 2826 MB ribbons [$Fe_{40}Ni_{38}Mo_4B_{18}$] the crystallization temperature is at around 683 K [14, 15]. The reduced crystallization temperature in the case of thin films is due to the depletion of metalloids. The diffraction pattern of the annealed samples at 473 and 573 K shows a peak centred at 44° which can be assigned to the FCC phase of Fe–Ni.

The as-deposited and annealed films were also investigated by TEM. Figure 4(*a*) shows the bright field image of the as-deposited thin films. The microstructure exhibits a contrast typical of an amorphous material. The electron diffraction pattern (figure 5(*a*)) consists of a wide diffraction ring corresponding to an interplanar distance $d = 2.014$ Å. This corresponds to an average distance (x_m) between atoms in the amorphous structure, where $x_m = 1.23d = 2.5$ Å. This value is in agreement with the observations of Dunlop *et al* [16] in Finemet alloys.

Figures 4(*b*), (*c*) and (*d*) show the bright field images of the films annealed at 473 K, 573 K and 673 K, respectively. The microstructure consists of fine nanocrystallites embedded in an amorphous phase. Grain growth is observed with an increase in the annealing temperature. The selected area diffraction pattern (figure 5(*b*)) confirms that these are nanocrystallites of the Fe–Ni phase which is consistent with our XRD observations. The EDS point analysis on the nanocrystals showed that they are of $Fe_{57}Ni_{43}$ composition. The mean grain size (D) as estimated from the bright field image is around 10, 16 and 20 nm for samples annealed at 473, 573 and 673 K. There is also a ring corresponding to Fe_3O_4 or Fe_2O_3. It is not possible to differentiate between these two oxide phases by electron diffraction because of their structural

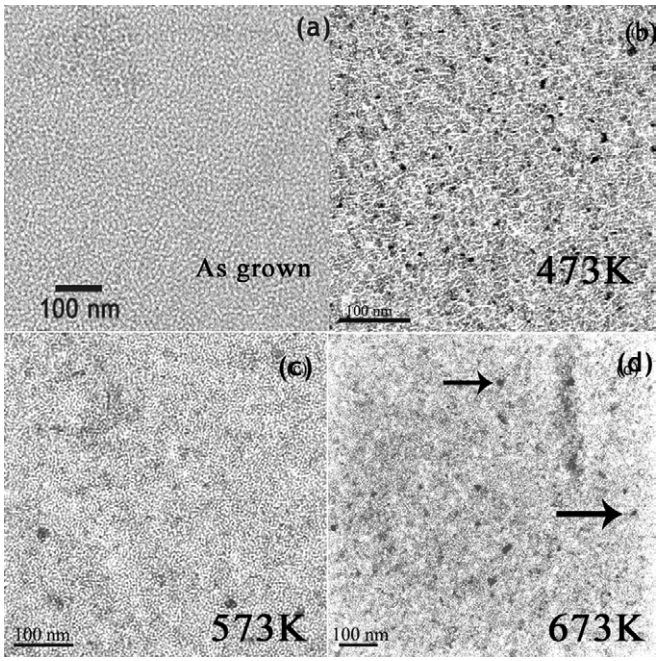

Figure 4. TEM bright field image of (*a*) as-deposited film and films annealed at (*b*) 473 K, (*c*) 573 K and (*d*) 673 K. The arrow in (*d*) points to the nanocrystalline precipitates.

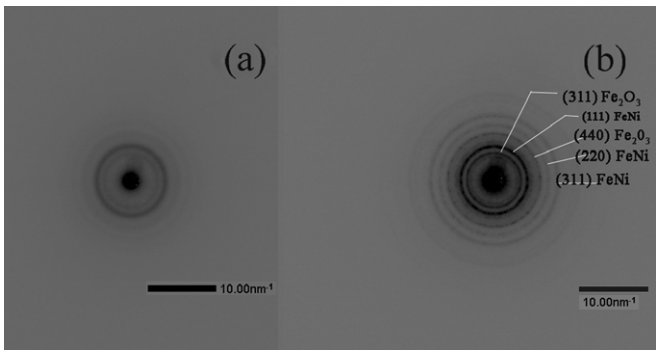

Figure 5. Electron diffraction pattern of (*a*) as-deposited film and (*b*) film annealed at 473 K.

similarities (inverse spinel). However, the Fe 2p XPS spectrum (figure 6) shows that the oxide formed is that of Fe_2O_3. The Fe $2p_{3/2}$ peak occurs at around 710 eV which indicates the presence of Fe_2O_3 on the surface of the film. The curve fitting shows that the Fe 2p peak can be resolved into two components with their binding energies centred at 710 eV and 707 eV which corresponds to Fe^{3+} and Fe°, respectively [17]. The absence of oxide peaks in the XRD pattern implies that their percentage concentration is very low well below the detection limits of XRD. Since we were not employing any capping agents against oxidation the formation of a native oxide layer on the surface of the films cannot be ruled out.

2.5. STM and STS studies

Figures 7(*a*) and (*b*) show the STM image of the as-deposited and 673 K annealed film, respectively. The topography reveals an island-like structure which implies that the film grows according to the Volmer–Weber model [18]. According to

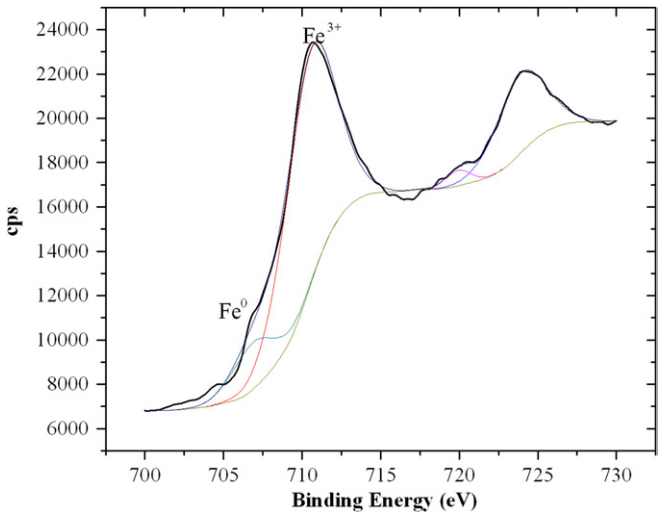

Figure 6. XPS Fe 2p spectrum.

this growth model the interaction between the adatoms will be greater than the interaction with the substrate. So the resultant will be a three-dimensional nucleus. The morphology of such films will exhibit island-like features. The AFM line scan in figure 7(*c*) illustrates the 3D nature of the growth. *I*–*V* characteristics were measured in the STS mode at ten different places on the sample surface with the same set point current. Figures 8(*a*) and (*b*) show *I*–*V* graphs representing two different behaviours in the 673 K annealed film. It is clear that the zero current gap is narrower in figure 8(*a*) than that in figure 8(*b*). Also the magnitude of the tunnelling current is considerably enhanced in figure 8(*a*) than that in figure 8(*b*). These observations point to the electronic inhomogeneity in the 673 K annealed sample. This can be correlated with the microstructural observations. The TEM bright field image of the 673 K annealed samples showed the coexistence of crystalline and amorphous phases. The crystalline phase which is more conducting than the amorphous phase is responsible for the behaviour in figure 8(*a*) while the amorphous phase is responsible for that in figure 8(*b*). Further *I*–*V* characteristics of the as-deposited amorphous sample (figure 8(*c*)) support this argument where one can notice a wide zero current gap similar to that in figure 8(*b*).

2.6. Magnetic studies

Figure 9 shows the hysteresis loops for the as-deposited and annealed films measured in a field parallel to the film's plane. It is to be noted here that there is a marked difference in the observed coercivity of the as-deposited and annealed films.

The variation of coercivity with annealing temperature is plotted and is shown in figure 10. It is evident from the graph that softening occurs at around 373 K before the onset of crystallization. This is because of the stress relief from the amorphous matrix. From 473 K onwards the coercivity shows a strong dependence on the grain size. It is to be noted that nanocrystallization occurs at around 473 K and TEM images show that grain growth is facilitated at higher annealing temperatures. The coercivity increased from 36 to 107 Oe as the grain size increased from 10 to 20 nm.

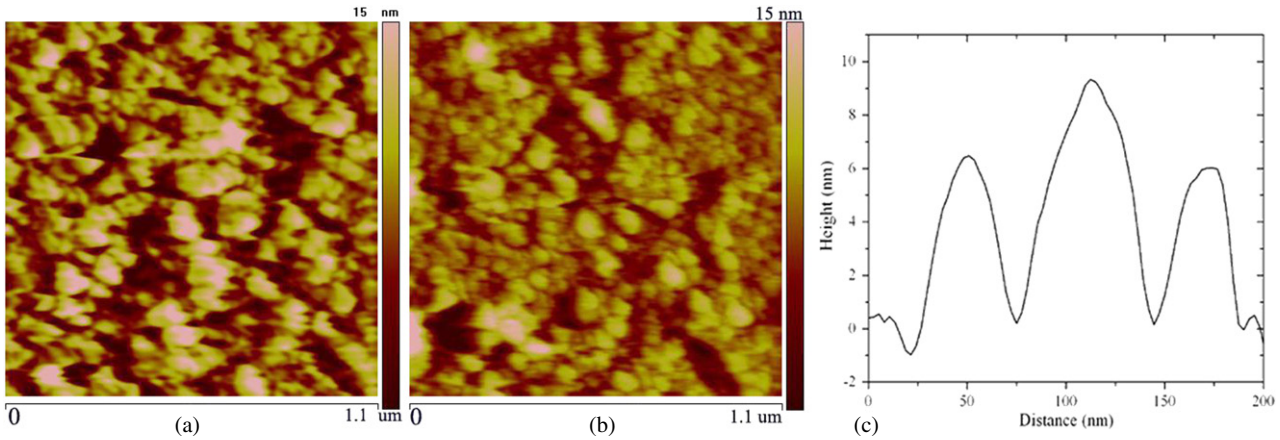

Figure 7. STM image of (*a*) as-deposited and (*b*) 673 K annealed films. (*c*) A line scan indicating the 3D nature of the growth.

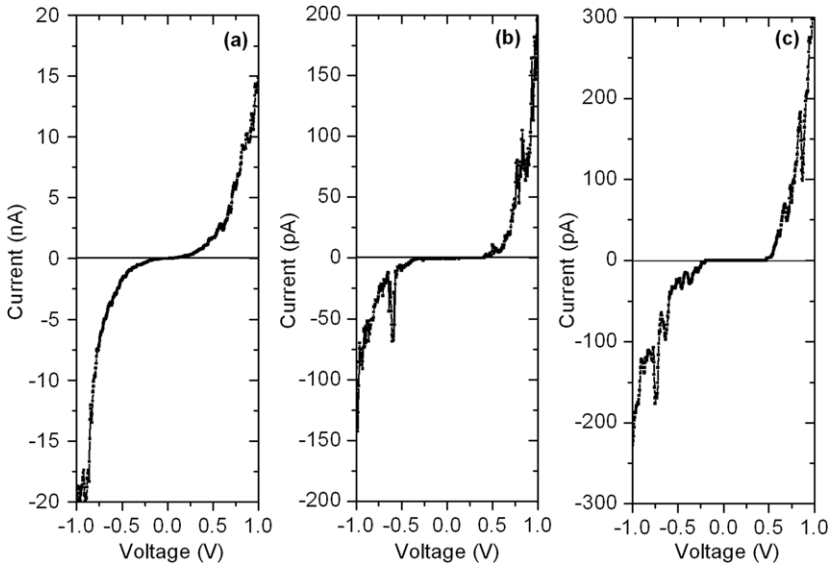

Figure 8. *I–V* characteristics for 673 K annealed films (*a*) from the crystalline phase, (*b*) from an amorphous interlayer and (*c*) from an as-deposited thin film.

The coercivity in nanocrystalline ferromagnetic films can also be described by the random anisotropy model [5]. When the grain size D is smaller than the exchange length L_{ex}, the effective anisotropy affecting the magnetization process results from averaging over the N ($N = (L_{ex}/D)^3$) grains within the volume ($V = L_{ex}^3$) of the exchange length. Therefore, $\langle K \rangle$ can be written as

$$\langle K \rangle = \frac{K_1}{\sqrt{N}} = K_1 \left(\frac{D}{L_{ex}} \right)^{3/2}. \tag{1}$$

Substituting $\langle K \rangle$ for K_1 in the equation for L_{ex} we get

$$L_{ex} = \sqrt{\frac{A}{\langle K \rangle}}. \tag{2}$$

This renormalization of L_{ex} results from the interplay of anisotropy and exchange energy. The combination of (1) and (2) gives

$$\langle K \rangle \sim \frac{K_1}{A^3} D^6, \tag{3}$$

which holds when the grain size D is smaller than the exchange length (L_{ex}). The most significant feature of the above analysis is the strong variation of $\langle K \rangle$ with the sixth power of the grain size. Using the results for coherent spin rotation [5] coercivity is related to $\langle K \rangle$ as

$$H_c = p_c \frac{\langle K \rangle}{M_S} \sim \frac{p_c K_1 D^6}{M_S A^3}, \qquad (D < L_{ex}), \tag{4}$$

where K_1 is the magnetocrystalline anisotropy constant, M_s is the saturation magnetization, A is the exchange constant and p_c is a dimensionless quantity related to the crystal structure.

If one of the dimensions of the nanocrystalline material is smaller than the exchange correlation length (L_{ex}), the averaging effect of anisotropies can be confined to two dimensions. Then

$$\langle K \rangle = \frac{K_1}{\sqrt{N}} = K_1 \left(\frac{D}{L_{ex}} \right). \tag{5}$$

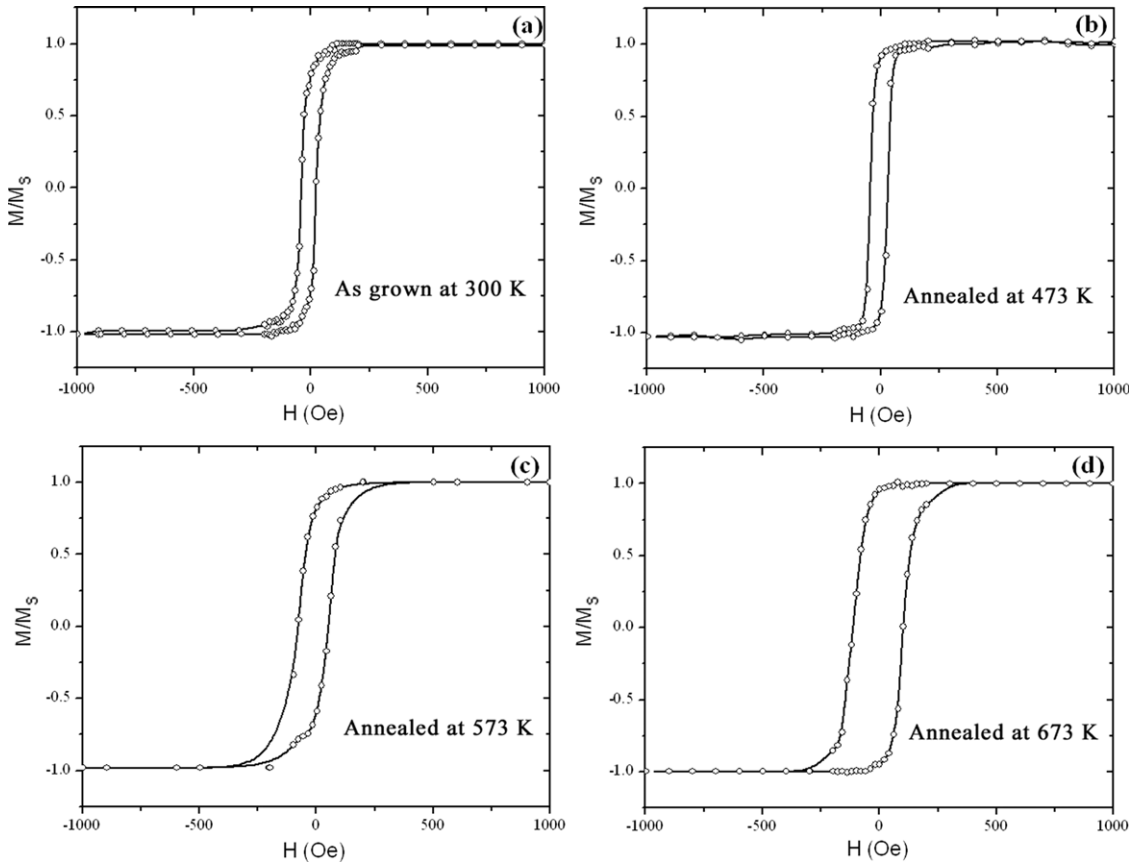

Figure 9. Room temperature hysteresis loop of (*a*) as-deposited and films annealed at (*b*) 473 K, (*c*) 573 K and (*d*) 673 K measured in a parallel field.

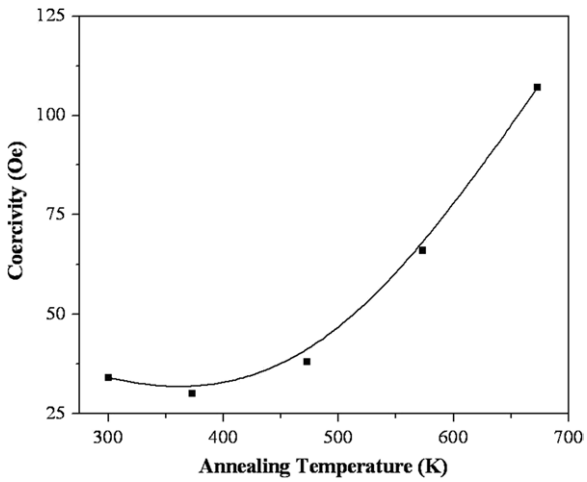

Figure 10. Coercivity dependence on the annealing temperature. Solid line is a guide to the eye.

Substituting (2) in (5) we get

$$\langle K \rangle = \frac{K_1^2}{A} D^2. \tag{6}$$

And therefore

$$H_c = p_c \frac{\langle K \rangle}{M_S} \sim \frac{p_c K_1^2 D^2}{M_S A}. \tag{7}$$

This equation suggests that for two-dimensional systems the Herzers D^6 law has to be replaced by the D^2 law.

The experimental dependence of H_c on the grain size, D, is shown in figure 11. The solid line is a linear fit to the experimental points. The slope of the curve was found to be ∼1.5. One can notice that there is a discrepancy in experimental and theoretical slopes. It should be noted that while deriving the D^2 law we have assumed a single value for the grain size D. But the electron micrographs show that there is a distribution in the grain size, D. The inhomogeneity in the grain size has a pronounced effect on the effective anisotropy [19]. This could be one of the reasons for the discrepancy observed in the theoretical and experimental slopes. Local magnetic anisotropy can be evaluated using the equation $H_c = p_c K_1^2 D^2 / M_S A$. Substitute the values for M_s ($M_s = 861\,\mathrm{emu\,cm^{-3}}$), A ($A = 10^{-11}\,\mathrm{J\,m^{-1}}$) and assume $p_c = 0.6$. The anisotropy constant K_1 was calculated from the slope of the H_c versus D^2 plot. The value of K_1 was found to be $5.7\,\mathrm{kJ\,m^{-3}}$. This value is slightly greater than the reported values for bulk FeNi with similar composition ($1\,\mathrm{kJ\,m^{-3}}$) [20]. This enhancement can be attributed to the surface anisotropy that is reported in ultra-fine particles [21]. Knowing the value of K_1 and A one can determine L_{ex} using the equation $L_{ex} = \sqrt{A/K_1}$. The value of L_{ex} is found to be 40 nm. The film thickness in this investigation is well below the exchange length which supports the applicability of the two-dimensional random anisotropy model to the films in the current investigation.

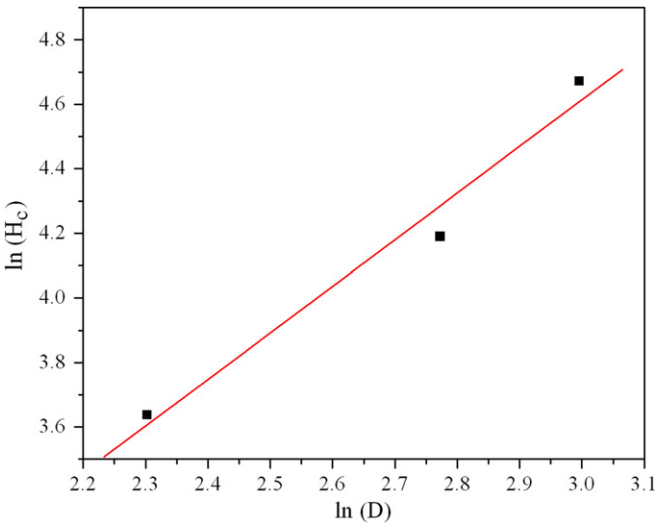

Figure 11. Dependence of H_c on the grain size D.

3. Conclusion

Vapour deposited thin films of Fe–Ni were thermally annealed to obtain a nanocrystalline microstructure. Electron microscopy and STM investigations showed that the microstructure consisted of Fe–Ni nanocrystals embedded in an amorphous matrix. The size of the nanocrystals was controlled by annealing the films at different temperatures. The coercivity had a strong dependence on the grain size. The observed grain size dependence of the coercivity is attributed to the random magnetic anisotropy characteristic of the system and was explained using the random anisotropy model extended to two-dimensional systems.

Acknowledgments

This work is supported by the Inter University Accelerator Centre, New Delhi, India, through the UGC Funded University Project, UFUP No 35306. Fruitful discussions with Mr Hysen Thomas and Dr Ratheesh Kumar P M is gratefully acknowledged. Al-Omari would like to thank the Sultan Qaboos University for the support under Grant number IG-SCI-PHYS-07-05.

References

[1] Wang S X, Sun N X, Yamaguchi M and Yabukami S 2000 *Nature* **407** 150
[2] Yong L and Arokia N 1997 *Appl. Phys. Lett.* **70** 526
[3] Hasegawa R 2004 *Mater. Sci. Eng.* A **375** 90
[4] Alben R, Becker J J and Chi M C 1978 *J. Appl. Phys* **49** 1653
[5] Herzer G 1990 *IEEE Trans. Magn.* **26** 1397
[6] Herzer G 1991 *Mater. Sci. Eng.* A **133** 1
[7] McHenry M E, Willard M A and Laughlin D E 1999 *Prog. Mater. Sci.* **44** 291
[8] Hernando A, Marín P, López M, Kulik T, Varga L K and Hadjipanayis G 2004 *Phys. Rev.* B **69** 052501
[9] Hono K and Ohnuma M 2002 *Magnetic Nanostructures* ed H S Nalwa (Los Angeles, CA: American Scientific Publishers) p 327
[10] Yoshizawa Y, Oguma S and Yamauchi K 1988 *J. Appl. Phys.* **64** 6044
[11] Idzikowski B, Szajek A, Greneche J M and Kovac J 2004 *Appl. Phys. Lett.* **85** 1392
[12] Mastrogiacomo G, Kradolfer J and Löffler J F 2006 *J. Appl. Phys.* **99** 023908
[13] Jyothi M and Suryanarayana C 1985 *Z. Metallk.* **76** 802
[14] Hysen T, Deepa S, Saravanan S, Ramanujan R V, Avasthi D K, Joy P A, Kulkarni S D and Anantharaman M R 2006 *J. Phys. D: Appl. Phys.* **39** 1993
[15] Du S W and Ramanujan R V 2004 *Mater. Sci. Eng.* A **375** 1040
[16] Dunlop A, Jaskierowicz G, Rizza G and Kopcewicz M 2003 *Phys. Rev. Lett.* **90** 015503
[17] Moulder J F, Stickle W F, Sobol P E and Bomben K D 1992 *Handbook of X-ray Photoelectron Spectroscopy* ed J Chastain (MN: Perkin-Elmer Corporation) p 222
[18] Hawkeye M M and Brett M J 2007 *J. Vac. Sci. Technol.* A **25** 1317
[19] Teruo B, Akihiro M and Akihisa I 2004 *J. Magn. Magn. Mater.* **272** 1445
[20] Chikazumi S 1997 *Physics of Ferromagnetism* (New York: Oxford Science Publications) p 287
[21] Kita E, Tsukuhara N, Sato H, Ota K, Yangaihara H, Tanimoto H and Ikeda N 2006 *Appl. Phys. Lett.* **88** 152501